Cryo-EM reveals mechanistic insights into lipid-facilitated polyamine export by human ATP13A2

Atsuhiro Tomita[1], **Takashi Daiho**[2], **Tsukasa Kusakizako**[1], **Keitaro Yamashita**[3], **Satoshi Ogasawara**[4], **Takeshi Murata**[4], **Tomohiro Nishizawa**[1,5,*], **Osamu Nureki**[1,6,*]

[1]Department of Biological Sciences, Graduate School of Science, The University of Tokyo, 7-3-1 Hongo, Bunkyo-ku, Tokyo 113-0033, Japan

[2]Department of Biochemistry, Asahikawa Medical University, Midorigaoka-Higashi, Asahikawa 078-8510, Japan

[3]MRC Laboratory of Molecular Biology, Francis Crick Avenue, Cambridge CB2 0QH, UK

[4]Department of Chemistry, Graduate School of Science, Chiba University, 1-33 Yayoi-cho, Inage-ku, Chiba 263-8522, Japan

[5]Graduate School of Medical Life Science, Yokohama City University, 1-7-29, Tsurumi, Yokohama 230-0045, Japan

Summary

The cytoplasmic polyamine maintains cellular homeostasis by chelating toxic metal cations, regulating transcriptional activity, and protecting DNA. ATP13A2 was identified as a lysosomal polyamine exporter responsible for polyamine release into the cytosol, and its dysfunction is associated with Alzheimer's disease and other neural degradation diseases. ATP13A2 belongs to the P5 subfamily of the P-type ATPase family, but its mechanisms remain unknown. Here, we report the cryoelectron microscopy (cryo-EM) structures of human ATP13A2 under four different conditions, revealing the structural coupling between the polyamine binding and the dephosphorylation. Polyamine is bound at the luminal tunnel and recognized through numerous electrostatic and p-cation interactions, explaining its broad specificity. The unique N-terminal domain is anchored to the lipid membrane to stabilize the E2P conformation, thereby accelerating the E1P-to-E2P transition. These findings reveal the distinct mechanism of P5B ATPases, thereby paving the way for neuroprotective therapy by activating ATP13A2.

Abstract

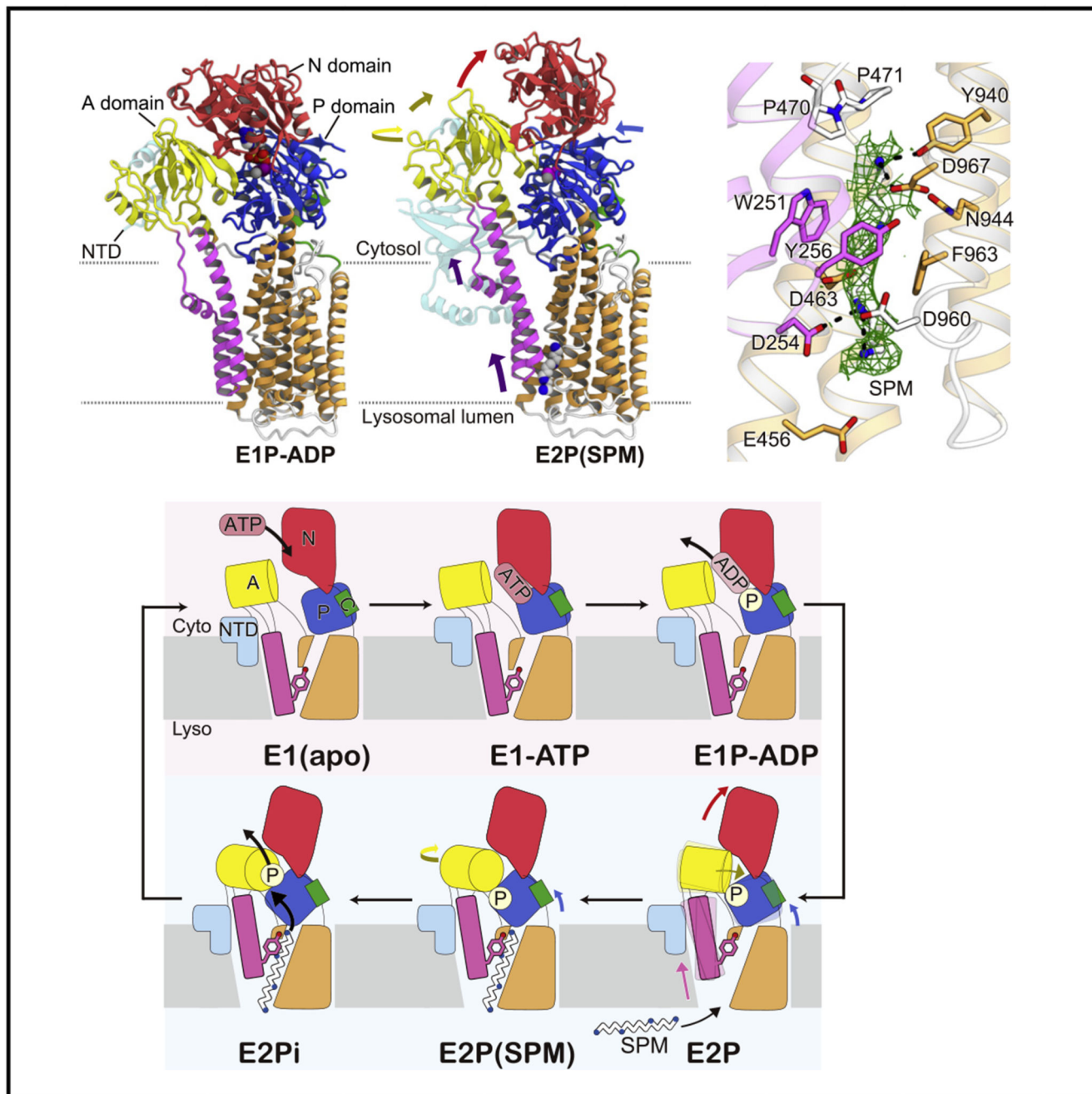*Correspondence: t-2438@yokohama-cu.ac.jp (T.N.), nureki@bs.s.u-tokyo.ac.jp (O.N.).
[6]Lead contact

Graphical abstract. In brief

Tomita et al. report the cryo-EM structure of ATP13A2 in E1-ATP, E1P-ADP, SPM-bound E2P (E2P(SPM)), and SPM-bound E2Pi (E2Pi(SPM)) states. These structures together with molecular dynamics simulation reveal the transport mechanism of polyamine by ATP13A2.

Introduction

Polyamines are essential organic compounds for maintaining various biological activities in all eukaryotes (Tabor and Tabor, 1984; Marton and Pegg, 1995). Among the various polyamine species, spermine (SPM) plays especially important roles in cells, such as interacting with nucleic acids to regulate transcriptional activity (Kanemura et al., 2018), stabilizing chromatin structure (Snyder, 1989; Feuerstein et al., 1990), and protecting DNA (Brüne et al., 1991; Khan et al., 1992a, 1992b). In addition, intracellular SPM protects cells from damage caused by reactive oxygen species (ROS) (Ha et al., 1998; Li et al., 2017). Accordingly, abnormalities in cellular SPM homeostasis lead to various diseases, including neurological disorders (Li et al., 2017). Cellular SPM homeostasis is maintained by both the intracellular biosynthetic pathway and SPM uptake from external sources (Minois et al., 2011). As the amount of intracellular SPM biosynthesis decreases with aging, the pathway for external SPM uptake is important for maintaining cellular functions (Minois et al., 2011). Recently, the P-type ATPase of type V subfamily B (P5B-ATPase) ATP13A2 was identified as the lysosomal poly-amine exporter that plays a crucial role in SPM release to the cytoplasm (van Veen et al., 2020). Several mutations in ATP13A2 are also associated with Parkinson's disease (Ramirez et al., 2006; Dehay et al., 2012).

ATP13A2 belongs to the P-type ATPase family, which is a major group of ion and lipid pumps found in all organisms (van Veen et al., 2014). The P-type ATPases are classified into 5 major subtypes (P1–P5) that share a similar architecture composed of cytoplasmic ATPase domains (A, actuator domain; N, nucleotide-binding domain; and P, phosphorylation domain) and a transmembrane region, although their transport substrates and physiological roles vary (Palmgren and Nissen, 2011). The P1–P3 ATPases generally transport metal cations and protons. The P2 subtype includes a sarcoplasmic reticulum Ca^{2+} pump (SERCA) (Olesen et al., 2004, 2007; Toyoshima et al., 2004, 2007), Na^+/K^+-ATPase (Shinoda et al., 2009; Toyoshima, 2009; Kanai et al., 2013; Nyblom et al., 2013), and H^+/K^+-ATPase (Abe et al., 2018), and a considerable number of structural and biochemical studies have elucidated their transport mechanism. Also, for the P1 and P3 subtypes, their structures have been reported previously (Pedersen et al., 2007; Gourdon et al., 2011). The P4 and P5 ATPases have been recently identified as non-metal-cationic, large substrate transporters.

P4 ATPases transport lipids (Montigny et al., 2016), P5 ATPases transport a broader range of substrates. The two subclades of the P5 ATPases, P5A and P5B, have totally different physiological substrates: P5A ATPases catalyze the dislocation of incorrectly delivered peptides (α helix dislocase) (McKenna et al., 2020), whereas P5B ATPases, which include ATP13A2, transport polyamines (van Veen et al., 2020). The molecular mechanisms of these "large substrate" P-type ATPases have been a long-standing question since their discovery. Recent structural studies of P4 ATPases have elucidated their unique mechanisms of lipid recognition and flipping (Hiraizumi et al., 2019; Timcenko et al., 2019; Bai et al., 2020; Nakanishi et al., 2020a, 2020b). With regard to P5 ATPases, only the structures of P5A ATPases are available (McKenna et al., 2020), while those of P5B ATPases have remained unsolved; therefore, the mechanism of polyamine transport by P5B ATPases remains unknown. Here, we report the cryoelectron microscopy (cryo-EM)

structures of human ATP13A2 under four different conditions: the non-hydrolyzable ATP analog AMPPCP-bound state, E1-ATP; the ADP-Pi (Pi, inorganic phosphate) analog AlF_4^--ADP-bound state, E1P-ADP; the BeF_3^--bound state in complex with SPM, E2P(SPM); and the AlF_4^--bound state in complex with SPM, E2Pi(SPM). These structures, together with biochemical and computational analyses, have revealed the unique mechanisms of polyamine recognition and transport by ATP13A2.

Results

Overall structure

To understand the molecular mechanisms of P5B ATPases, we performed a cryo-EM analysis of the human P5B ATPase poly-amine exporter ATP13A2 (Figure 1). The N-terminally GFP-tagged, full-length human ATP13A2 was expressed in human embryonic kidney 293 (HEK293) cells, and the microsomes prepared from the cells showed SPM-dependent ATPase activity (Figure 1C). The ATP13A2 protein was purified in glycol diosgenin (GDN) and subjected to cryo-EM single-particle analyses under several different conditions, in the presence of AMPPCP, AlF_4^--ADP, BeF_3^-, and AlF_4^- (Figures S1-S4; Table 1). The acquired videos were motion corrected and processed in RELION 3.1 (Zivanov et al., 2018), which eventually provided cryo-EM maps at overall resolutions of 3.54–3.92 Å, according to the gold-standard Fourier shell correlation (FSC) 0.143 criterion (Figures S1-S4). The cytoplasmic ATPase domains are well resolved in the AMPPCP-and BeF_3^--bound states, thus allowing *de novo* modeling of the almost entire ATP13A2 structure, except for some minor disordered regions (residues 1–33; 114–160; 587–595; 611–617; 798–819; and 1,174–1,180 in the BeF_3^--bound state and residues 1–179; 590–595; 611–617; 798–819; and 1,174–1,180 in the AMPPCP-bound state), and these models were used as the template for the modeling of other states (Figure 1B; Figure S5; Data S1). The overall structure shows the typical P-type ATPase fold, composed of three large cytoplasmic domains (A, N, and P) and ten membrane-spanning helices (M1–M10) (Figures 1A and 1B). ATP13A2 has extra C-terminal and N-terminal domains (CTD and NTD, respectively), which are not present in other P-type ATPases. The CTD adopts a short α helix that lines and stabilizes the P domain, whereas the NTD is extended from the A domain and anchored to the lipid membrane (Figure 1B). According to the hydropathy plot, the NTD contains a pair of short membrane-embedded helices (Holemans et al., 2015), but density of this region is weak and almost disordered in the AMPPCP- and AlF_4^--ADP-bound states. A similar NTD structure was also observed in a yeast P5A-ATPase (McKenna et al., 2020), and the NTD structure is likely to be a common feature in the P5 ATPases, based on the amino acid sequence alignment (Data S1).

Ligand-binding cavity and transport pathway

ATP13A2 generally follows the Post-Albers scheme (Albers, 1967; Post et al., 1969) (Figure 2A). In this model, ATP-dependent autophosphorylation and polyamine-dependent dephosphorylation alternately induce the transition of the different enzymatic states, referred as E1 and E2, and consequently allow polyamine transport. The cryo-EM maps revealed the densities of the respective inhibitors at the catalytic site, which stabilize the ATPase domains in respective conformations (Figures 2A and 2B). The AMPPCP-and AlF_4^--bound

structures, which correspond to the E1-ATP and E1P-ADP states, respectively, represent the ATP-dependent autophosphorylation step in the Post-Albers scheme (Figure 2A). The ATP analog is recognized by the conserved motifs.

The adenine ring interacts with Phe630 of the N domain, whereas the γ-phosphate group interacts with Asp513 and Thr515 (DKTG motif), Asn881, and Asp878 at the phosphorylation site of the P domain, in cooperation with a Mg^{2+} ion (E1-ATP and E1P-ADP in Figure 2B). All of these domains adopt the same rearrangement in the $AlF_4{}^-$-ADP-bound structure, but the N and P domains are more tightly bridged by ADP and $AlF_4{}^-$. The two structures are almost identical, with a 0.99 Å root-mean-square deviation (RMSD) and both represent the E1 state (Figure S5E), which is defined as a low-affinity state to the substrate polyamines. By contrast, the two phosphate analogs, $BeF_3{}^-$ and $AlF_4{}^-$, captured ATP13A2 in the substrate-bound E2P(SPM) (modeled as a likely substrate) and E2Pi(SPM) states, respectively (Figures 3A-3C; Figures S5C and S5D). $BeF_3{}^-$ is covalently attached to the carboxylate side chain of Asp513, in coordination with a Mg^{2+} ion, and tethers the A domain to the phosphorylation site through the backbone carbonyls of Thr346 and Gly347 in the conserved TGES motif (E2P(SPM) in Figure 2B). $AlF_4{}^-$ similarly occupies the phosphorylation site (E2Pi(SPM) in Figure 2B). Because of the moderate resolutions of the two structures, it was difficult to determine the exact coordination of $BeF_3{}^-$ and $AlF_4{}^-$. Therefore, we modeled these analogs according to the previous high-resolution structures of other P-type ATPases bound to the same analogs. The two structures are almost identical, with a 0.80 Å RMSD and both represent the E2 state (Figure S5G), which is defined as a high-affinity state to the substrate polyamines.

In both E2P(SPM) and E2Pi(SPM) structures, a long tunnel is created between the M1−M2 and M4−M5 segments, in which an elongated density probably corresponding to substrate polyamine was observed (Figure 3A; Figure S6A). This tunnel is rendered electronegative by several carboxylate residues, such as Asp254, Asp463, Asp960, and Asp967, and polyamine is directly recognized by these residues and additionally by aromatic residues, such as Trp251, Tyr256, Tyr940, and Phe963 (Figures 3B and 3C). The observed elongated density is likely SPM added to the specimen, as similarly observed in the recently reported structure of yeast homologous protein (Li et al., 2021). However, we cannot exclude the possibility of SPD or other endogenous poly-amines contaminated in the sample. The substrate-binding cavity of ATP13A2 is larger than those of P2-type ATPases, such as SERCA (Sørensen et al., 2004), and a P4-ATPase (ATP8A1) (Hiraizumi et al., 2019), but rather smaller than that of P5A ATPase (yeast Spf1) (McKenna et al., 2020), which is suggested to catalyze the translocation of α-helical peptides (Figures S6B-S6E).

To assess the functional roles of the residues constituting the substrate-binding cavity of ATP13A2, we measured the ATPase activities of their mutants. Almost all ATP13A2 mutants showed decreased SPM-dependent ATPase activity, while retaining the ability to form EP (phosphoenzyme) (Figures 3D and 3E), confirming the integrity of the mutant proteins and thus revealing their substantial contributions to the ATPase activity. In general, the transport substrate of P-type ATPases is recognized by specific interactions near the central TM4 kink (Toyoshima et al., 2000; Shinoda et al., 2009; Nyblom et al., 2013; Abe et al., 2018; Hiraizumi et al., 2019). By contrast, in ATP13A2, SPM is recognized by

broad interactions through several negatively charged and aromatic residues surrounding the luminal tunnel (Figure 3B). This recognition manner is unique in ATP13A2 and explains its broad specificity, with the preference for longer poly-amine species (van Veen et al., 2020).

Polyamine transport mechanism

The structural comparison of the E2P (SPM) (BeF$_3$ $^-$) and E1P-ADP (AlF$_4$ $^-$-ADP) states revealed the conformational changes upon the E1-to-E2 transition: a large dislocation of the N domain, an inclination of the P domain against the membrane plane, and upward (toward the cytoplasmic side) and rotational movements of the A domain (Figure 4A; Figure S5F; Video S1). The rearrangement of these cytoplasmic domains induces extensive rearrangements in the TM region; specifically, a slight inclination of the cytoplasmic portions of the M5 and M4b segments and a large upward and rotational movement of the M1–M2 segments (Figure 4B). The latter changes in the M1–M2 segments directly induce the luminal gate opening, by creating a tunnel between the M1–M2 and M4–M5 segments and thereby allowing SPM entry (Figures 5A and 5B).

In most P-type ATPases, substrate binding from the extracellular/luminal side (protons in SERCA, phospholipids in P4-ATPase) involves sequential steps (Figures 5C and 5D) through the E1P, E2P, and E2Pi intermediates, which structurally involve the A domain rearrangement toward the phosphorylation site, and the binding of substrates. While the first step is coupled to (or induced by) the phosphorylation, the extracellular/luminal substrate binding in the second step is coupled to the dephosphorylation reaction (Figure 6) (Olesen et al., 2004, 2007; Toyoshima et al., 2007). The two phosphate analogs, BeF$_3$ $^-$and AlF$_4$ $^-$, have different coordination geometries, which accordingly allow the enzyme to be captured in different intermediate states; namely, the phosphorylated E2 state (E2P) and its hydrolyzed intermediate (E2Pi) (Figures 6C and 6D) (Olesen et al., 2007; Toyoshima et al., 2007; Hiraizumi et al., 2019). In SERCA, the dephosphorylation reaction during this E2P-to-E2Pi transition is coupled to the luminal proton binding (and simultaneous Ca^{2+} release into the lumen), which involves the rearrangement of the hydrogen-bonding network in the substrate-binding site (Figures 5C and 6C) (Olesen et al., 2007; Toyoshima et al., 2007). In P4-ATPase (ATP8A1), phospholipid binding only induces the sliding of the M1–M2 segments, which is coupled to the A domain rear-rangement and thus facilitates dephosphorylation (Figures 5D and 6D). However, in ATP13A2 the current BeF$_3$ $^-$- and AlF$_4$ $^-$-stabilized SPM-bound structures are essentially the same, including the A domain orientation toward the P domain (Figures S5C and S5D). Furthermore, Glu348 (TGES motif) is in the proximity of the phosphoryl group attached to Asp513 (DKTG motif) in both structures, which is a signature coordination for dephosphorylation (E2P(SPM) and E2Pi(SPM) in Figure 2B). Considering the SPM-dependent ATPase activity of ATP13A2, it is most likely that the substrate binding stabilizes the M1–M2 segments and the A domain in their current positions, to facilitate the dephosphorylation reaction (Figures 6A and 6B). MD simulations using the structure of the E2P(SPM) state as the initial model revealed that the M1–M2 segments adopt flexible conformations in the absence of SPM, but become stabilized with the SPM in the positions observed in the cryo-EM structures (Figure S7), further supporting our notion. It should also be noted that, in ATP13A2, Tyr259 on the M2 segment, participating in the hydrogen-bonding network in the E1 state,

dislocates upon the E2 transition and constitutes the luminal tunnel for the SPM binding (Figures 5A and 5B), suggesting that it plays an essential role in the SPM-dependent dephosphorylation. Consistently, the mutation of Tyr259 greatly decreases the ATPase activity of ATP13A2 (Figure 3D). These results together indicate that the M1−M2 segments serve as the "connector" that enables the structural coupling between the polyamine binding and the A domain rearrangement in ATP13A2. This mechanism somewhat resembles that of ATP8A1, as it also induces the M1−M2 shift upon phospholipid binding (Figure 6D), consistent with the evolutional relationship between the P4 and P5 subfamilies (Videos S2 and S3).

ATP13A2 has a unique NTD and CTD, which are both likely to contribute to the structural stability. However, while the NTD deletion severely affects the EP formation, the CTD deletion only moderately affects the EP formation (Figure 3E), suggesting their distinct roles. The NTD contains several clusters of positively charged residues, which presumably constitute binding sites for PA and PIP_2 (Data S1) (Holemans et al., 2015). The current structures reveal the proximity of these residues to the lipid boundary (Figure 7A). According to the previous study, phosphorylated ATP13A2 preferentially adopts the E1P conformation, but supplementation with these lipids advances the reaction cycle to the E2P conformation (Holemans et al., 2015). Therefore, the binding of specific lipids, such as PA and PIP_2, probably stabilizes the interaction of the NTD with the lipid membrane and thereby affects the E1P-to-E2P transition upon phosphorylation (Figure 7B). Consistently, the NTD is visible only in the E2P conformations (BeF_3^- and AlF_4^-), whereas it is almost completely disordered in the E1 conformations (AMPPCP and AlF_4^--ADP) (Figure S5), indicating the role of the NTD in the stabilization of the E2P conformation, although we cannot rule out the possibility that it is merely an artifact derived from the GDN micelles.

In the current SPM-bound structures, SPM is stuck at the central kink in the M4 helix and still exposed to the lumen (Figures 3B and 3C). According to our simulation, the water solvent access cavity is discrete near the M4 kink, and the polyamine-permeating tunnel is sealed on the cytoplasmic side by several lipid molecules (Figures S8A-S8D). Therefore, further conformational changes are required to transport SPM completely to the cytoplasmic side. ATP13A2 has two sequential Pro residues, which create a larger M4 kink, whereas other P-type ATPases have only a single Pro residue at the corresponding position (Figures S9A-S9C). Yeast P5A ATPase (Spf1) similarly has two Pro residues and undergoes a large sliding of the cytoplasmic M4b segment upon substrate transport (Figure S9D). Our mutation analysis has illustrated the cytoplasmic exit pathway of ATP13A2 (Figure 3D; Figure S8). For example, mutations of the hydrophilic and aromatic residues on the M2 helix, such as Tyr241 and Gln244, decreased the SPM-dependent ATPase activity (Figure 3D). Altogether, these results suggest that SPM is transported along the cleft between the M1−M2 and M4−M6 helices, and this transport is probably associated with the sliding of the cytoplasmic M4b segment that restricts the exit pathway in the current E2P and E2Pi structures (Figures S8E and S8F).

Discussion

ATP13A2 consists of a general P-type ATPase fold and additional NTDs and CTDs. While the overall architecture is similar to that of yeast P5A-ATPase (Spf1), there are significant differences between the two P5 ATPase clades, P5A and P5B. First, each transporter adopts the suitable binding-cavity conformation for the respective substrate. ATP13A2 has a long negatively charged tunnel for polyamine permeation, whereas Spf1 would have a wide cavity beside the TM segments, which enables the translocation of incredibly large a-helical peptide substrates (Figure S6) (McKenna et al., 2020). Most notably, the current structures of ATP13A2 revealed that the NTD adopts a stable conformation only in the E2P state with its hydrolyzed intermediate, E2Pi, thus highlighting its role in facilitating the E1P-to-E2P transition. The NTD is likely to activate the transport activity by stabilizing the high-affinity state for the polyamines. Furthermore, the facilitating role of the NTD is accelerated by the binding of specific lipids, such as PA and PIP_2, and the activation switching by these lipids is implicated in the protection from mitochondria stress and thus in Parkinson's disease (Holemans et al., 2015). While the NTD is commonly conserved in the P5 ATPases, this regulatory role of the NTD is only proposed in the P5B ATPases, including ATP13A2, and not in the P5A ATPases, indicating the distinct functions between the two subclades. Furthermore, the current findings may offer a rational strategy for neuroprotective therapy, by activating ATP13A2.

Limitation of the study

First, our assay of the SPM-dependent ATPase activity in microsomes showed an unexpected inhibition by high-concentration SPM, which is not reported previously. It seems that the transport and/or ATPase activity of ATP13A2 could be affected by several factors, such as specific lipid binding to the NTD. The result might also suggest unidentified regulators contaminated in the microsomes sample. Complicated regulation in cellular context would be the remaining issues in the studies of P5-ATPases.

Second, probably due to the flexible nature of ATP13A2 in GDN micelles, only the two distinct conformations could be captured, even under four different conditions. Most notably, the two phosphate analogs, BeF_3^- and AlF_4^-, capture ATP13A2 in the almost same conformations, corresponding to the SPM-bound hydrolyzing intermediate, indicating the high flexibility of ATP13A2 in the E2P conformation without polyamines. In addition, the elongated shape of the density in such moderate resolution maps is not sufficient to identify detailed interactions and to understand precise mechanism for the polyamine recognition. Particularly, the structural information upon substrate release to the cytosol is completely lacking. Therefore, further investigation of structural and biochemical studies is required.

Star⋆Methods

Detailed methods are provided in the online version of this paper and include the following:

- KEY RESOURCES TABLE
- RESOURCE AVAILABILITY

○ Lead contact

○ Materials availability

○ Data and code availability

• EXPERIMENTAL MODEL AND SUBJECT DETAILS

○ Cell lines

• METHOD DETAILS

○ Expression and purification of the ATP13A2

○ Electron microscopy preparation

○ Electron microscopy data collection

○ Image processing

○ Model building and refinement

○ ATPase activity assay

○ Molecular dynamics simulation

• QUANTIFICATION AND STATISTICAL ANALYSIS

Star⋆Methods

Key Resources Table

REAGENT or RESOURCE	SOURCE	IDENTIFIER
Antibodies		
GFP enhancer nanobody	Kirchhofer et al., 2010	PDB: 3K1K
Bacterial and virus strains		
Baculovirus	Thermo Fisher Scientific	10359016
Chemicals, peptides, and recombinant proteins		
Freestyle 293 medium	GIBCO	12338-018
Sf9-900 II SFM	GIBCO	10902-088
Spermine	Sigma-Aldrich	85590
N-dodecyl β-D-maltoside	Calbiochem	69227-93-6
Cholesteryl hemisuccinate	Anatrace	CH210
glyco-diogenin	Anatrace	GDN101
Ni-NTA Superflow resin	QIAGEN	30410
CNBr-activated Sepharose 4 Fast Flow Lab Packs	GE Healthcare Life Science	17098101
Superose 6 Increase 10/300 GL column	GE Healthcare	29091596
300 mesh R 1.2/1.3 holey carbon Cu/Rh	Quantifoil	https://www.quantifoil.com/products/quantifoil/quantifoil-circular-holes/
Critical commercial assays		
Bac-to-Bac Baculovirus Expression System	Invitrogen	A11098
Deposited data		
ATP13A2 coordinate (E1-ATP state)	This paper	PDB: 7VPI
ATP13A2 coordinate (E1P-ADP state)	This paper	PDB: 7VPJ
ATP13A2 coordinate (E2P(SPM) state)	This paper	PDB: 7VPK
ATP13A2 coordinate (E2Pi(SPM) state)	This paper	PDB: 7VPL
ATP13A2 map (E1-ATP state)	This paper	EMDB: EMD-32066
ATP13A2 map (E1P-ADP state)	This paper	EMDB: EMD-32067
ATP13A2 map (E2P(SPM) state)	This paper	EMDB: EMD-32068
ATP13A2 map (E2Pi(SPM) state)	This paper	EMDB: EMD-32069
Structure of the (SR) Ca²⁺-ATPase Ca2-E1-ADP:AlF₄⁻ form	Sørensen et al., 2004	PDB: 1T5T
SERCA Ca²⁺-ATPase E2 aluminum fluoride complex without thapsigargin	Olesen et al., 2007	PDB: 3B9R

REAGENT or RESOURCE	SOURCE	IDENTIFIER
Cryo-EM structure of the human P4-type flippase ATP8A1-CDC50 (E1-ADP-Pi state)	Hiraizumi et al., 2019	PDB: 6K7K
Cryo-EM structure of the human P4-type flippase ATP8A1-CDC50 (E2Pi-PL state)	Hiraizumi et al., 2019	PDB: 6K7M
Structure of P5A-ATPase Spf1, endogenous substrate-bound	McKenna et al., 2020	PDB: 6XMU
Cryo-EM structure of the human P4-type flippase ATP8A1-CDC50 (E1-ATP state class1)	Hiraizumi et al., 2019	PDB: 6K7J
Structure of the (SR) Ca^{2+}-ATPase Ca2-E1-AMPPCP form	Sørensen et al., 2004	PDB: 1T5S
Structure of P5A-ATPase Spf1, AMP-PCP-bound form	McKenna et al., 2020	PDB: 6XMQ
Structure of P5A-ATPase Spf1, BeF3-bound form	McKenna et al., 2020	PDB: 6XMT
Structure of the E2 beryllium fluoride complex of the SERCA Ca^{2+}-ATPase	Olesen et al., 2007	PDB: 3B9B
Experimental models: Cell lines		
HEK293S GnTI$^-$		N/A
Oligonucleotides		
Primers for ATP13A2 mutants, see Table S1	This paper	N/A
Recombinant DNA		
pEGNGFP-HumanATP13A2	This paper	N/A
pET22b-GFP binding nanobody	This paper	N/A
Software and algorithms		
Refmac5	Nicholls et al., 2018	https://www.mrc-lmb.cam.ac.uk/groups/murshudov/content/refmac/refmac.html
ProSMART	Nicholls et al., 2012	https://www.mrc-lmb.cam.ac.uk/groups/murshudov/content/prosmart/prosmart.html
Servalcat	Yamashita et al., 2021	https://github.com/keitaroyam/servalcat
COOT	Emsley et al., 2010; Nicholls et al., 2018	https://www.mrc-lmb.cam.ac.uk/personal/pemsley/coot/
PHENIX	Afonine et al., 2018	https://phenix-online.org/
MolProbity	Chen et al., 2010	https://phenix-online.org/documentation/reference/molprobity_tool.html
UCSF-ChimeraX	Goddard et al., 2018	https://www.cgl.ucsf.edu/chimerax/
CueMol	N/A	http://www.cuemol.org
VMD	Humphrey et al., 1996	http://www.ks.uiuc.edu/Research/vmd/
MemProtMD	Stansfeld et al., 2015	http://memprotmd.bioch.ox.ac.uk/
CHARMM-GUI	Jo et al., 2008; Kim et al., 2017	https://www.charmm-gui.org/
NAMD2.13	Phillips et al., 2005	http://www.ks.uiuc.edu/Research/namd/

Resource Availability

Lead contact

Further information and requests for resources and reagents should be directed to and will be fulfilled by the Lead Contact, Osamu Nureki (nureki@bs.s.u-tokyo.ac.jp).

Experimental Model and Subject Details

Cell lines

Sf9 cells (GIBCO Thermo Fisher, Loughborough, UK, Cat. No. 11496-015) were cultured in Sf9-900 II SFM (GIBCO Cat. No. 10902-088) at 27°C. These cells were used for production of baculovirus. HEK293S GnTI– (N-acetylglucosaminyl-transferase I–negative) cells (American Type Culture Collection, Teddington, UK, Cat. No. CRL-3022) were cultured in FreeStyle 293 expression medium (GIBCO Cat. No. 12338-018) supplemented with 2% (v/v) heat-inactivated fetal bovine serum (NICHIREI, Tokyo, Japan, Cat. No. 174012).

Method Details

Expression and purification of the ATP13A2

The human ATP13A2 transcription variant 2 (Uniprot: Q9NQ11-2) cDNA was purchased from Kazusa DNA Research Institute. The human ATP13A2 cDNA was cloned into the pEG BacMam vector, with an N-terminal His$_8$ tag and enhanced green fluorescent protein (EGFP), followed by a human rhinovirus 3C protease (HRV3C protease) recognition site.

HEK293S GnTI⁻(N-acetylglucosaminyl-transferase I–negative) cells (American Type Culture Collection, catalog no. CRL-3022) were infected at a density of 3.0 3 10^6 cells mL^{-1} with one-hundredth volume of a solution containing the virus encoding the above construct. The infected HEK293S cells were incubated in FreeStyle 293 Expression medium (GIBCO) with 2% fetal bovine serum (Sigma), at 37°C in the presence of 8% CO_2. After 8-12 h, 10 mM valproic acid (Sigma) was added, and the cells were further incubated at 30°C in the presence of 8% CO_2 for 48 h. The cells were collected by centrifugation (5,000 3 g, 10 min, 4°C) and lysed in buffer, containing 50 mM Tris (pH 8.0), 150 mM NaCl, 5 mM DTT, and 20% (v/v) glycerol. The collected cells were solubilized for 1 h at 4°C in buffer, containing 50 mM Tris (pH 8.0), 150 mM NaCl, 1.5% (w/v) N-dodecyl β-D-maltoside (DDM), 0.15% (w/v) cholesterol hemisuccinate CHS, 5 mM DTT, and 20% (v/v) glycerol. After ultracentrifugation, the supernatant was incubated with AffiGel 10 (Bio-Rad) coupled with a GFP-binding nanobody for 1 h at 4°C. The resin was washed five times with four column volumes of wash buffer, containing 50 mM Tris (pH 8.0), 300 mM NaCl, 1.5% (w/v) glyco-diogenin (GDN), 5 mM DTT, and 20% (v/v) glycerol, and then gently suspended overnight with HRV3C Protease to cleave the His$_8$-EGFP tag. After HRV3C protease digestion, the flow-through was collected, mixed with Ni-NTA Superflow resin (QIAGEN) and incubated for 1 min at 4°C to remove the HRV3C protease. The collected flowthrough was then concentrated using an Amicon Ultra filter (molecular mass cut-off 100 kDa, Millipore), and further purified by chromatography on a gel filtration

column (Superose 6 Increase 10/300 GL, GE Healthcare) equilibrated with gel filtration buffer, containing 20 mM Tris (pH 8.0), 150 mM NaCl, 1.5% (w/v) glyco-diogenin (GDN), and 5 mM DTT. The peak fractions of the protein were pooled and concentrated to ~10 mg mL^{-1} with a centrifugal device (Millipore 30 kDa MW cutoff).

Electron microscopy preparation

The purified ATP13A2 was mixed with inhibitor at the following final concentrations: E1-ATP, 5 mM MgCl$_2$ and 2 mM AMPPCP; E1P-ADP, 5 mM MgCl$_2$, 5 mM NaF, 1 mM AlCl$_3$, and 5 mM ADP; E2P(SPM), 5 mM spermine, 5 mM MgCl$_2$, 10 mM NaF, and 2 mM BeSO$_4$; E2Pi(SPM), 5 mM spermine, 5 mM MgCl$_2$, 10 mM NaF, and 2 mM AlCl$_3$. After an incubation for 1 h on ice, the protein solutions were applied to a freshly glow-discharged Quantifoil holey carbon grid (R1.2/1.3, Cu/Rh, 300 mesh), using a Vitrobot Mark IV (FEI) at 4°C with a blotting time of 4 s under 99% humidity conditions, and then the grids were plunge-frozen in liquid ethane.

Electron microscopy data collection

The grids with the E1-ATP and E1P-ADP samples were transferred to a Titan Krios G3i microscope (Thermo Fisher Scientific), running at 300 kV and equipped with a Gatan Quantum-LS Energy Filter (GIF) and a Gatan K3 Summit direct electron detector, operated in the electron counting mode. Imaging was performed at a nominal magnification of 105,000 ×, corresponding to a calibrated pixel size of 0.83 Å/pix (The University of Tokyo, Japan). Each movie was recorded for 2.55 s and subdivided into 48 frames. The electron flux was set to 14 e$^-$/s at the detector, resulting in an accumulated exposure of 50 e$^-$/Å^2 at the specimen. The data were automatically acquired by the image shift method using the SerialEM software (Mastronarde, 2005), with a defocus range of −0.8 to −1.6 μm. More than 3,500 movies were acquired for each grid condition, and the numbers of total images are described in Table S1.

The grids of the E2P(SPM) and E2Pi(SPM) samples were transferred to a Titan Krios G3i microscope (Thermo Fisher Scientific), running at 300 kV and equipped with a Gatan Quantum-LS Energy Filter (GIF) and a Gatan K3 Summit direct electron detector, operated in the electron counting CDS mode. Imaging was performed at a nominal magnification of 105,000 ×, corresponding to a calibrated pixel size of 0.83 Å/pix (The University of Tokyo, Japan). Each movie was recorded for 5.96 s and subdivided into 64 frames. The electron flux was set to 7.55 e$^-$/s at the detector, resulting in an accumulated exposure of 60 e$^-$/Å^2 at the specimen. The data were automatically acquired by the image shift method using the SerialEM software (Mastronarde, 2005), with a defocus range of −0.8 to −1.6 μm. More than 3,000 movies were acquired for each grid condition, and the numbers of total images are described in Table S1.

Image processing

For all datasets, the dose-fractionated movies were subjected to the beam-induced motion correction implemented in RELION-3.1 (Zivanov et al., 2018), and the contrast transfer function (CTF) parameters were estimated using CTFFIND4 (Rohou and Grigorieff, 2015).

For the E1-ATP state in the presence of AMPPCP, 1,989,286 particles were initially picked from the 3,114 micrographs by using the Laplacian-of-Gaussian picking function in RELION-3.1 (Zivanov et al., 2018), and extracted with down-sampling to a pixel size of 3.32 Å/pix. These particles were subjected to several rounds of 2D and 3D classifications. The best class contained 345,121 particles, which were then re-extracted with a pixel size of 1.51 Å/pix and subjected to 3D refinement. The resulting 3D model and particle set were subjected to per-particle defocus refinement, beam-tilt refinement, Bayesian polishing (Zivanov et al., 2019), micelle subtraction and 3D refinement. The final 3D refinement and postprocessing of the three classes yielded a map with a global resolution of 3.6 Å, according to the FSC = 0.143 criterion (Rosenthal and Henderson, 2003). The local resolution was estimated by RELION-3.1.

The processing strategy is described in Figures S1A-S1C. For the E1P-ADP state dataset in the presence of AlF_4^- and ADP, 1,950,094 particles were initially picked from the 3,303 micrographs, and extracted with down-sampling to a pixel size of 3.32 Å/ pix, as described above. These particles were subjected to three rounds of 3D classifications. The best class from the 3D classifi-cation contained 121,731 particles, which were then re-extracted with a pixel size of 1.51 Å/pix and subjected to 3D refinement, using a soft mask covering the proteins and micelles. The resulting 3D model and particle set were subjected to per-particle CTF refinement, beam-tilt refinement, and Bayesian polishing before the final 3D refinement and postprocessing, yielding a map with a global resolution of 3.5 Å according to the Fourier shell correlation (FSC) = 0.143 criterion. Finally, the local resolution was estimated using RELION-3. The processing strategy is described in Figures S2A-S2C. For the E2P(SPM) state in the presence of BeF_3^-, 1,762,758 particles were initially picked from the 3,289 micrographs, and extracted with a pixel size of 3.37 Å/pix, as described above. These particles were subjected to several rounds of 3D classifications. The best class from the 3D classification contained 22,952 particles, which were then re-extracted with a pixel size of 1.68 Å/pix and subjected to 3D refinement. The resulting 3D model and particle set were subjected to Bayesian polishing and 3D refinement. The final 3D refinement and postprocessing of the best particles yielded a map with a global resolution of 3.9 Å, according to the FSC = 0.143 criterion. The local resolution was estimated using RELION-3. The processing strategy is described in Figures S3A-S3C. For the E2Pi(SPM) state in the presence of AlF_4^-, 1,958,257 particles were initially picked from the 3,834 micrographs, and extracted with a pixel size of 3.24 Å/pix, as described above. These particles were subjected to several rounds of 3D classification. The best class from the 3D classification contained 53,403 particles, which were then re-extracted with a pixel size of 1.68 Å/pix and subjected to 3D refinement. The resulting 3D model and particle set were subjected to Bayesian polishing and 3D refinement. The final 3D refinement and postprocessing of the best particles yielded a map with a global resolution of 3.8 Å, according to the FSC = 0.143 criterion. The local resolution was estimated, and the processing strategy is described in Figures S4A-S4C.

Model building and refinement

The quality of the density maps of the E1-ATP and E2P(SPM) states was sufficient to build a model manually in COOT (Emsley et al., 2010). These models were used as the template

for the modeling of other states. The model building was facilitated by the crystal structure of the sodium - potassium pump (PDB ID 2ZXE) (Shinoda et al., 2009) and previous crystal structures of SERCA (PDB IDs 3B9B, 3B9R) (Olesen et al., 2007) and cryo-EM structures of P5A ATPase Spf1 (PDB IDs 6XMQ, 6XMT) (McKenna et al., 2020). The model building was also facilitated by maps postprocessed by deepEMhancer (Sanchez-Garcia et al., 2020), a deep learning-based post-processing tool. For the NTD, the model predicted by RaptorX (Xu et al., 2021) was fitted into the map and manually adjusted with COOT. After manual adjustment of the models, structure refinement was performed with phenix.real_space_refine ver. 1.18 (Afonine et al., 2018). The refined models were further processed using Refmac5 (Nicholls et al., 2018) and servalcat (Yamashita et al., 2021) with ProSMART (Nicholls et al., 2012) distance restraints generated from the cryo-EM structures of P5A ATPase Spf1 (PDB 6XMQ, 6XMT) (McKenna et al., 2020) as the templates. The sequence alignment was generated using HHpred (Söding et al., 2005) server and the models were prepared using phenix.mr_model_preparation. The statistics of the 3D reconstruction and model refinement are summarized in Table S1. All molecular graphics figures were prepared with CueMol (http://www.cuemol.org) and UCSF ChimeraX (Goddard et al., 2018).

ATPase activity assay

The rate of ATP hydrolysis was determined at 37°C for 30 min in 10 mL of a mixture containing 0.8 μg of microsomal protein, 1 mM [γ-^{32}P]ATP, 0.125 mM PIP$_2$, 0.125 mM PA, various concentrations of SPM, 200 mM KCl, 5 mM DTT, 0.03% GDN, and 20 mM MOPS/KOH (pH 7.0). The reaction was chased by the addition of HCl, and the released ^{32}P$_i$ was quantified as described previously (Daiho et al., 2001). The SPM dependence (Figure 1C) was calculated by the least fitting of ATPase activities to the complex Hill equation.

$$v = V_{\max}\left(\frac{1}{1+\left(\frac{K_1}{[SPM]}\right)^{n_1}}\right)\left(1-\frac{1}{1+\left(\frac{K_2}{[SPM]}\right)^{n_2}}\right)$$

To measure the amount of EP formation at steady state without substrate, phosphorylation of ATP13A2 in microsomes with [γ-^{32}P] ATP was performed under conditions described in the figure legends essentially as described previously (Daiho et al., 2001). The amount of EP was determined by acid quenching. Precipitated proteins were separated by 5% SDS-PAGE at pH 6.0. The radioactivity associated with the separated ATP13A2 was quantified by digital autoradiography. The amount of EP for expressed ATP13A2 was obtained by subtracting the background radioactivity determined with the microsomes from the mock-transfected cells. The background radioactivity was less than 9% of the total radioactivity of the microsomes expressing wild-type ATP13A2.

Molecular dynamics simulation

The system included the ATP13A2, SPM, 1-phosphoryl-2-oleoylphosphatidylcholine (POPC), TIP3P water and 150 mM NaCl. The initial model of ATP13A2 containing amino acids 191-1173 was created with MODELER (Sali and Blundell, 1993), using the cryo-EM structure of ATP13A2 in E2P(SPM) or E2Pi(SPM) state as the template. The missing

hydrogen atoms were built with the program VMD (Humphrey et al., 1996). The protein was embedded into the POPC membrane, using the MemProtMD pipeline (Stansfeld et al., 2015). The net charge of the simulation system was neutralized through the addition of 150 mM NaCl. The simulation system was 120 3 120 3 144 $\mathring{A}^3$ and contained 185,180 atoms. The molecular topologies and parameters from the Charmm36 force field (Klauda et al., 2010; Best et al., 2012) were used for the protein, lipid, and water molecules. The molecular topology and parameters for SPM were prepared using the CHARMM-GUI ligand reader and modeler (Jo et al., 2008; Kim et al., 2017).

Molecular dynamics simulations were performed with the program NAMD 2.13. The simulation systems were energy minimized for 1,000 steps with fixed positions of the non-hydrogen atoms. After minimization, another 1,000 steps of energy minimization were performed with 10 kcal mol^{-1} restraints for the non-hydrogen atoms, except for the lipid molecules within 5.0 Å of the proteins. Next, equilibrations were performed for 0.1 ns under NVT conditions, with 10 kcal mol^{-1}Å ^{2} restraints for the heavy atoms of the proteins. Finally, equilibration was performed for 2.0 ns under NPT conditions, with the 1.0 kcal mol^{-1}Å ^{2} restraints for all Cα atoms of the proteins. The production runs were performed for 200 ns without restraints, while maintaining constant temperature at 310K using Langevin dynamics and constant pressure at 1 atm using a Nosé-Hoover Langevin piston (Feller et al., 1995). The long-range electrostatic interactions were calculated by the particle mesh Ewald method (Darden et al., 1993). The simulations were performed twice each for the E2P state in the absence of SPM, E2P state in the presence of SPM, and E2Pi state in the presence of SPM. The simulation results were analyzed and visualized with mdtraj (McGibbon et al., 2015), seaborn (https://zenodo.org/record/54844), and CueMol (http://www.cuemol.org).

Quantification and Statistical Analysis

The data represent the mean SD for 3–6 independent experiments. Statistical analysis was performed by one-way analysis of variance with Dunnett's post hoc test using SPSS software version 22.

Supplementary Material

Refer to Web version on PubMed Central for supplementary material.

Acknowledgments

Data and code availability

- Coordinates for AMPPCP-, AlF$_4$ $^-$-ADP-, BeF$_3$ $^-$, and AlF$_4$ $^-$-bound ATP13A2 have been deposited as 7VPI, 7VPJ, 7VPK, and 7VPL, respectively. EM-maps

for AMPPCP-, AlF_4^--ADP-, BeF_3^--, and AlF_4^--bound ATP13A2 have been deposited as EMD-32066, EMD-32067, EMD-32068, and EMD-32069, respectively.

- This paper does not report original code.

- Any additional information required to reanalyze the data reported in this paper is available from the lead contact upon request.

Materials availability

All unique/stable reagents generated in this study are available from the lead contact with a completed materials transfer agreement.

References

Abe K, Irie K, Nakanishi H, Suzuki H, Fujiyoshi Y. Crystal structures of the gastric proton pump. Nature. 2018; 556: 214–218. [PubMed: 29618813]

Afonine PV, Poon BK, Read RJ, Sobolev OV, Terwilliger TC, Urzhumtsev A, Adams PD. Real-space refinement in PHENIX for cryo-EM and crystallography. Acta Crystallogr D Struct Biol. 2018; 74: 531–544. [PubMed: 29872004]

Albers RW. Biochemical aspects of active transport. Annu Rev Biochem. 1967; 36: 727–756. [PubMed: 18257736]

Bai L, You Q, Jain BK, Duan HD, Kovach A, Graham TR, Li H. Transport mechanism of P4 ATPase phosphatidylcholine flippases. eLife. 2020; 9: 1–20.

Best RB, Zhu X, Shim J, Lopes PE, Mittal J, Feig M, Mackerell AD Jr. Optimization of the additive CHARMM all-atom protein force field targeting improved sampling of the backbone $\varnothing$, ψ and side-chain $\chi(1)$ and $\chi(2)$ dihedral angles. J Chem Theory Comput. 2012; 8: 3257–3273. [PubMed: 23341755]

Brüne B, Hartzell P, Nicotera P, Orrenius S. Spermine prevents endonuclease activation and apoptosis in thymocytes. Exp Cell Res. 1991; 195: 323–329. [PubMed: 1649056]

Chen VB, Arendall WB 3rd, Headd JJ, Keedy DA, Immormino RM, Kapral GJ, Murray LW, Richardson JS, Richardson DC. MolProbity : all-atom structure validation for macromolecular crystallography. Acta Crystallogr D Biol Crystallogr. 2010; 66: 12–21. [PubMed: 20057044]

Daiho T, Yamasaki K, Saino T, Kamidochi M, Satoh K, Iizuka H, Suzuki H. Mutations of either or both Cys876 and Cys888 residues of sarcoplasmic reticulum Ca2+-ATPase result in a complete loss of Ca2+ transport activity without a loss of Ca2+-dependent ATPase activity. Role of the CYS876-CYS888 disulfide bond. J Biol Chem. 2001; 276: 32771–32778. [PubMed: 11438520]

Darden T, York D, Pedersen L. Particle mesh Ewald: An N$log(N) method for Ewald sums in large systems. J Chem Phys. 1993; 98: 10089–10092.

Dehay B, Ramirez A, Martinez-Vicente M, Perier C, Canron MH, Doudnikoff E, Vital A, Vila M, Klein C, Bezard E. Loss of P-type ATPase ATP13A2/PARK9 function induces general lysosomal deficiency and leads to Parkinson disease neurodegeneration. Proc Natl Acad Sci USA. 2012; 109: 9611–9616. [PubMed: 22647602]

Emsley P, Lohkamp B, Scott WG, Cowtan K. Features and development of Coot. Acta Crystallogr D Biol Crystallogr. 2010; 66: 486–501. [PubMed: 20383002]

Feller SE, Zhang Y, Pastor RW. Constant pressure molecular dynamics simulation: The Langevin piston method. J Chem Phys. 1995; 103: 4613–4621.

Feuerstein BG, Pattabiraman N, Marton LJ. Molecular mechanics of the interactions of spermine with DNA: DNA bending as a result of ligand binding. Nucleic Acids Res. 1990; 18: 1271–1282. [PubMed: 2320418]

Goddard TD, Huang CC, Meng EC, Pettersen EF, Couch GS, Morris JH, Ferrin TE. UCSF ChimeraX: Meeting modern challenges in visualization and analysis. Protein Sci. 2018; 27: 14–25. [PubMed: 28710774]

Gourdon P, Liu XY, Skjørringe T, Morth JP, Møller LB, Pedersen BP, Nissen P. Crystal structure of a copper-transporting PIB-type ATPase. Nature. 2011; 475: 59–64. [PubMed: 21716286]

Ha HC, Sirisoma NS, Kuppusamy P, Zweier JL, Woster PM, Casero RA Jr. The natural polyamine spermine functions directly as a free radical scavenger. Proc Natl Acad Sci USA. 1998; 95: 11140–11145. [PubMed: 9736703]

Hiraizumi M, Yamashita K, Nishizawa T, Nureki O. Cryo-EM structures capture the transport cycle of the P4-ATPase flippase. Science. 2019; 365: 1149–1155. [PubMed: 31416931]

Ho BK, Gruswitz F. HOLLOW: generating accurate representations of channel and interior surfaces in molecular structures. BMC Struct Biol. 2008; 8: 49. [PubMed: 19014592]

Holemans T, Sørensen DM, van Veen S, Martin S, Hermans D, Kemmer GC, Van den Haute C, Baekelandt V, Günther Pomorski T, Agostinis P, et al. A lipid switch unlocks Parkinson's disease-associated ATP13A2. Proc Natl Acad Sci USA. 2015; 112: 9040–9045. [PubMed: 26134396]

Humphrey W, Dalke A, Schulten K. VMD: visual molecular dynamics. J Mol Graph. 1996; 14 (33–38) 27–28.

Jo S, Kim T, Iyer VG, Im W. CHARMM-GUI: a web-based graphical user interface for CHARMM. J Comput Chem. 2008; 29: 1859–1865. [PubMed: 18351591]

Kanai R, Ogawa H, Vilsen B, Cornelius F, Toyoshima C. Crystal structure of a Na^+-bound Na^+K^+-ATPase preceding the E1P state. Nature. 2013; 502: 201–206. [PubMed: 24089211]

Kanemura A, Yoshikawa Y, Fukuda W, Tsumoto K, Kenmotsu T, Yoshikawa K. Opposite effect of polyamines on In vitro gene expression: Enhancement at low concentrations but inhibition at high concentrations. PLoS ONE. 2018; 13 e0193595 [PubMed: 29494707]

Khan AU, Di Mascio P, Medeiros MH, Wilson T. Spermine and spermidine protection of plasmid DNA against single-strand breaks induced by singlet oxygen. Proc Natl Acad Sci USA. 1992a; 89: 11428–11430. [PubMed: 1454831]

Khan AU, Mei YH, Wilson T. A proposed function for spermine and spermidine: protection of replicating DNA against damage by singlet oxygen. Proc Natl Acad Sci USA. 1992b; 89: 11426–11427. [PubMed: 1454830]

Kim S, Lee J, Jo S, Brooks CL 3rd, Lee HS, Im W. CHARMM-GUI ligand reader and modeler for CHARMM force field generation of small molecules. J Comput Chem. 2017; 38: 1879–1886. [PubMed: 28497616]

Kirchhofer A, Helma J, Schmidthals K, Frauer C, Cui S, Karcher A, Pellis M, Muyldermans S, Casas-Delucchi CS, Cristina Cardoso M, et al. Modulation of protein properties in living cells using nanobodies. Nat Struct Mol Biol. 2010; 17: 133–138. [PubMed: 20010839]

Klauda JB, Venable RM, Freites JA, O'Connor JW, Tobias DJ, Mondragon-Ramirez C, Vorobyov I, MacKerell AD Jr, Pastor RW. Update of the CHARMM all-atom additive force field for lipids: validation on six lipid types. J Phys Chem B. 2010; 114: 7830–7843. [PubMed: 20496934]

Li C, Brazill JM, Liu S, Bello C, Zhu Y, Morimoto M, Cascio L, Pauly R, Diaz-Perez Z, Malicdan MCV, et al. Spermine synthase deficiency causes lysosomal dysfunction and oxidative stress in models of Snyder-Robinson syndrome. Nat Commun. 2017; 8 1257 [PubMed: 29097652]

Li P, Wang K, Salustros N, Grønberg C, Gourdon P. Structure and transport mechanism of P5B-ATPases. Nat Commun. 2021; 12 3973 [PubMed: 34172751]

Liu Y, Schmidt B, Maskell DL. MSAProbs: multiple sequence alignment based on pair hidden Markov models and partition function posterior probabilities. Bioinformatics. 2010; 26: 1958–1964. [PubMed: 20576627]

Marton LJ, Pegg AE. Polyamines as targets for therapeutic intervention. Annu Rev Pharmacol Toxicol. 1995; 35: 55–91. [PubMed: 7598507]

Mastronarde DN. Automated electron microscope tomography using robust prediction of specimen movements. J Struct Biol. 2005; 152: 36–51. [PubMed: 16182563]

McGibbon RT, Beauchamp KA, Harrigan MP, Klein C, Swails JM, Hernández CX, Schwantes CR, Wang LP, Lane TJ, Pande VS. MDTraj: A Modern Open Library for the Analysis of Molecular Dynamics Trajectories. Biophys J. 2015; 109: 1528–1532. [PubMed: 26488642]

McKenna MJ, Sim SI, Ordureau A, Wei L, Harper JW, Shao S, Park E. The endoplasmic reticulum P5A-ATPase is a transmembrane helix dislocase. Science. 2020; 369 eabc5809 [PubMed: 32973005]

Minois N, Carmona-Gutierrez D, Madeo F. Polyamines in aging and disease. Aging (Albany NY). 2011; 3: 716–732. [PubMed: 21869457]

Montigny C, Lyons J, Champeil P, Nissen P, Lenoir G. On the molecular mechanism of flippase- and scramblase-mediated phospholipid transport. Biochim Biophys Acta. 2016; 1861: 767–783. [PubMed: 26747647]

Nakanishi H, Irie K, Segawa K, Hasegawa K, Fujiyoshi Y, Nagata S, Abe K. Crystal structure of a human plasma membrane phospholipid flippase. J Biol Chem. 2020a; 295: 10180–10194. [PubMed: 32493773]

Nakanishi H, Nishizawa T, Segawa K, Nureki O, Fujiyoshi Y, Nagata S, Abe K. Transport Cycle of Plasma Membrane Flippase ATP11C by Cryo-EM. Cell Rep. 2020b; 32 108208 [PubMed: 32997992]

Nicholls RA, Long F, Murshudov GN. Low-resolution refinement tools in REFMAC5. Acta Crystallogr D Biol Crystallogr. 2012; 68: 404–417. [PubMed: 22505260]

Nicholls RA, Tykac M, Kovalevskiy O, Murshudov GN. Current approaches for the fitting and refinement of atomic models into cryo-EM maps using CCP-EM. Acta Crystallogr D Struct Biol. 2018; 74: 492–505. [PubMed: 29872001]

Nyblom M, Poulsen H, Gourdon P, Reinhard L, Andersson M, Lindahl E, Fedosova N, Nissen P. Crystal structure of Na$^+$K$^+$-ATPase in the Na$^+$-bound state. Science. 2013; 342: 123–127. [PubMed: 24051246]

Olesen C, Sørensen TL, Nielsen RC, Møller JV, Nissen P. Dephosphorylation of the calcium pump coupled to counterion occlusion. Science. 2004; 306: 2251–2255. [PubMed: 15618517]

Olesen C, Picard M, Winther AM, Gyrup C, Morth JP, Oxvig C, Møller JV, Nissen P. The structural basis of calcium transport by the calcium pump. Nature. 2007; 450: 1036–1042. [PubMed: 18075584]

Palmgren MG, Nissen P. P-type ATPases. Annu Rev Biophys. 2011; 40: 243–266. [PubMed: 21351879]

Pedersen BP, Buch-Pedersen MJ, Morth JP, Palmgren MG, Nissen P. Crystal structure of the plasma membrane proton pump. Nature. 2007; 450: 1111–1114. [PubMed: 18075595]

Phillips JC, Braun R, Wang W, Gumbart J, Tajkhorshid E, Villa E, Chipot C, Skeel RD, Kalé L, Schulten K. Scalable molecular dynamics with NAMD. J Comput Chem. 2005; 26: 1781–1802. [PubMed: 16222654]

Post RL, Kume S, Tobin T, Orcutt B, Sen AK. Flexibility of an active center in sodium-plus-potassium adenosine triphosphatase. J Gen Physiol. 1969; 54: 306–326. [PubMed: 19873651]

Ramirez A, Heimbach A, Gründemann J, Stiller B, Hampshire D, Cid LP, Goebel I, Mubaidin AF, Wriekat AL, Roeper J, et al. Hereditary parkinsonism with dementia is caused by mutations in ATP13A2, encoding a lysosomal type 5 P-type ATPase. Nat Genet. 2006; 38: 1184–1191. [PubMed: 16964263]

Robert X, Gouet P. Deciphering key features in protein structures with the new ENDscript server. Nucleic Acids Res. 2014; 42: W320–W324. [PubMed: 24753421]

Rohou A, Grigorieff N. CTFFIND4: Fast and accurate defocus estimation from electron micrographs. J Struct Biol. 2015; 192: 216–221. [PubMed: 26278980]

Rosenthal PB, Henderson R. Optimal determination of particle orientation, absolute hand, and contrast loss in single-particle electron cryomicroscopy. J Mol Biol. 2003; 333: 721–745. [PubMed: 14568533]

Šali A, Blundell TL. Comparative protein modelling by satisfaction of spatial restraints. J Mol Biol. 1993; 234: 779–815. [PubMed: 8254673]

Sanchez-Garcia R, Gomez-Blanco J, Cuervo A, Carazo J, Sorzano C, Vargas J. DeepEMhancer: A deep learning solution for cryo-EM volume post-processing. bioRxiv. 2020. 2020.06.12.148296

Shinoda T, Ogawa H, Cornelius F, Toyoshima C. Crystal structure of the sodium-potassium pump at 2.4 A resolution. Nature. 2009; 459: 446–450. [PubMed: 19458722]

Snyder RD. Polyamine depletion is associated with altered chromatin structure in HeLa cells. Biochem J. 1989; 260: 697–704. [PubMed: 2504149]

Söding J, Biegert A, Lupas AN. The HHpred interactive server for protein homology detection and structure prediction. Nucleic Acids Res. 2005; 33 (Suppl 2) W244–W248. [PubMed: 15980461]

Sørensen TLM, Møller JV, Nissen P. Phosphoryl transfer and calcium ion occlusion in the calcium pump. Science. 2004; 304: 1672–1675. [PubMed: 15192230]

Stansfeld PJ, Goose JE, Caffrey M, Carpenter EP, Parker JL, Newstead S, Sansom MS. MemProtMD: Automated Insertion of Membrane Protein Structures into Explicit Lipid Membranes. Structure. 2015; 23: 1350–1361. [PubMed: 26073602]

Tabor CW, Tabor H. Polyamines. Annu Rev Biochem. 1984; 53: 749–790. [PubMed: 6206782]

Timcenko M, Lyons JA, Januliene D, Ulstrup JJ, Dieudonné T, Montigny C, Ash MR, Karlsen JL, Boesen T, Kühlbrandt W, et al. Structure and autoregulation of a P4-ATPase lipid flippase. Nature. 2019; 571: 366–370. [PubMed: 31243363]

Toyoshima C. How Ca2+-ATPase pumps ions across the sarcoplasmic reticulum membrane. Biochim Biophys Acta. 2009; 1793: 941–946. [PubMed: 19010358]

Toyoshima C, Nakasako M, Nomura H, Ogawa H. Crystal structure of the calcium pump of sarcoplasmic reticulum at 2.6 A resolution. Nature. 2000; 405: 647–655. [PubMed: 10864315]

Toyoshima C, Nomura H, Tsuda T. Lumenal gating mechanism revealed in calcium pump crystal structures with phosphate analogues. Nature. 2004; 432: 361–368. [PubMed: 15448704]

Toyoshima C, Norimatsu Y, Iwasawa S, Tsuda T, Ogawa H. How processing of aspartylphosphate is coupled to lumenal gating of the ion pathway in the calcium pump. Proc Natl Acad Sci USA. 2007; 104: 19831–19836. [PubMed: 18077416]

van Veen S, Sørensen DM, Holemans T, Holen HW, Palmgren MG, Vangheluwe P. Cellular function and pathological role of ATP13A2 and related P-type transport ATPases in Parkinson's disease and other neurological disorders. Front Mol Neurosci. 2014; 27: 48.

van Veen S, Martin S, Van den Haute C, Benoy V, Lyons J, Vanhoutte R, Kahler JP, Decuypere JP, Gelders G, Lambie E, et al. ATP13A2 deficiency disrupts lysosomal polyamine export. Nature. 2020; 578: 419–424. [PubMed: 31996848]

Xu J, Mcpartlon M, Li J. Improved protein structure prediction by deep learning irrespective of co-evolution information. Nat Mach Intell. 2021; 3: 601–609. [PubMed: 34368623]

Yamashita K, Palmer CM, Burnley T, Murshudov GN. Cryo-EM single-particle structure refinement and map calculation using Servalcat. Acta Crystallogr D Struct Biol. 2021; 77: 1282–1291. [PubMed: 34605431]

Zivanov J, Nakane T, Forsberg BO, Kimanius D, Hagen WJ, Lindahl E, Scheres SH. New tools for automated high-resolution cryo-EM structure determination in RELION-3. eLife. 2018; 7 e42166 [PubMed: 30412051]

Zivanov J, Nakane T, Scheres SHW. A Bayesian approach to beam-induced motion correction in cryo-EM single-particle analysis. IUCrJ. 2019; 6: 5–17.

Highlights

- Cryo-EM structures of ATP13A2 under four different conditions

- Substrate polyamine is bound at the luminal tunnel

- Interactions essential for polyamine recognition are identified

- Structural dynamics during transport cycle of polyamine is revealed Authors
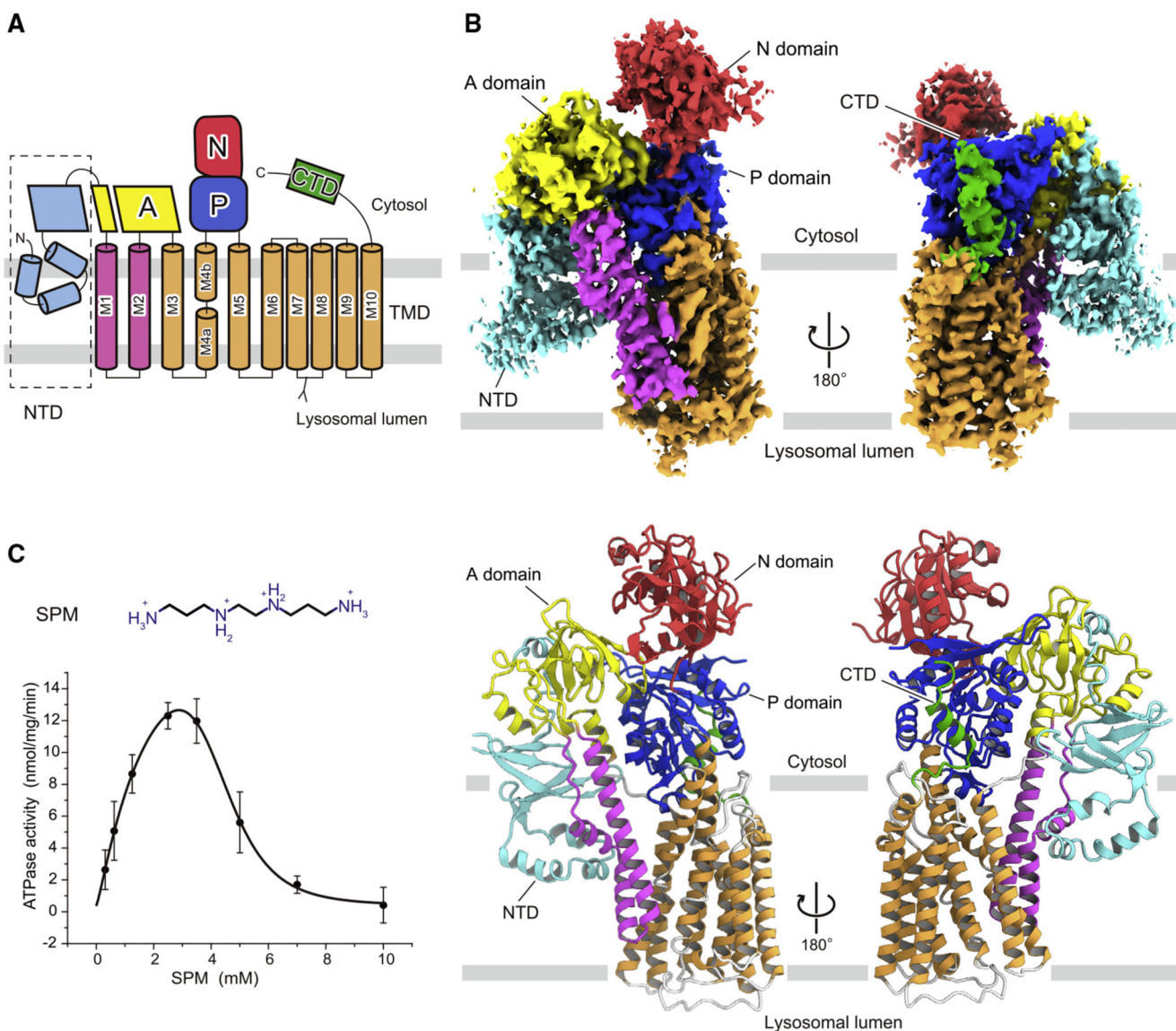
Figure 1. Structural and functional analyses of ATP13A2

(A) Topology diagram of human ATP13A2. Conserved domains and transmembrane (TM) helices are schematically illustrated. In the cytoplasmic regions, the A, N, and P domains, N-terminal domain (NTD), and the C-terminal domain (CTD) are colored yellow, red, blue, cyan, and green, respectively. M1–M2 and M3–M10 are pink and orange, respectively. The N-glycosylation site is shown as sticks.

(B) Overall structure of ATP13A2. Cryo-EM maps (top) and ribbon models (bottom), shown with the same color scheme as in (A).

(C) Chemical structural formula of spermine (SPM) (top) and dose-response curves (bottom) showing the SPM-dependent ATPase activities of ATP13A2-expressing microsomes. Phosphatidic acid (PA) and phosphatidylinositol 3,5-bisphosphate (PtdIns(3,5)P$_2$, PIP$_2$) were added to facilitate the ATPase activity of ATP13A2. Data points represent the mean ± SEM of three to six measurements. SPM-dependent ATPase activity of ATP13A2 was

measured by subtracting the ATPase activity in the absence of SPM. The solid line for the SPM dependence shows the least fit of ATPase activities (v) to the complex Hill equation (STAR Methods). The obtained K_1, K_2, and Hill coefficients n_1, n_2 were 1.7 ± 0.5, 4.5 ± 0.1 mM, and 1.2 ± 0.2, 5.9 ± 0.5, respectively. $V_{\max}$ is 20.0 ± 3.7 nmol mg^{-1} min^{-1}. See also Figures S1-S5 and Data S1.
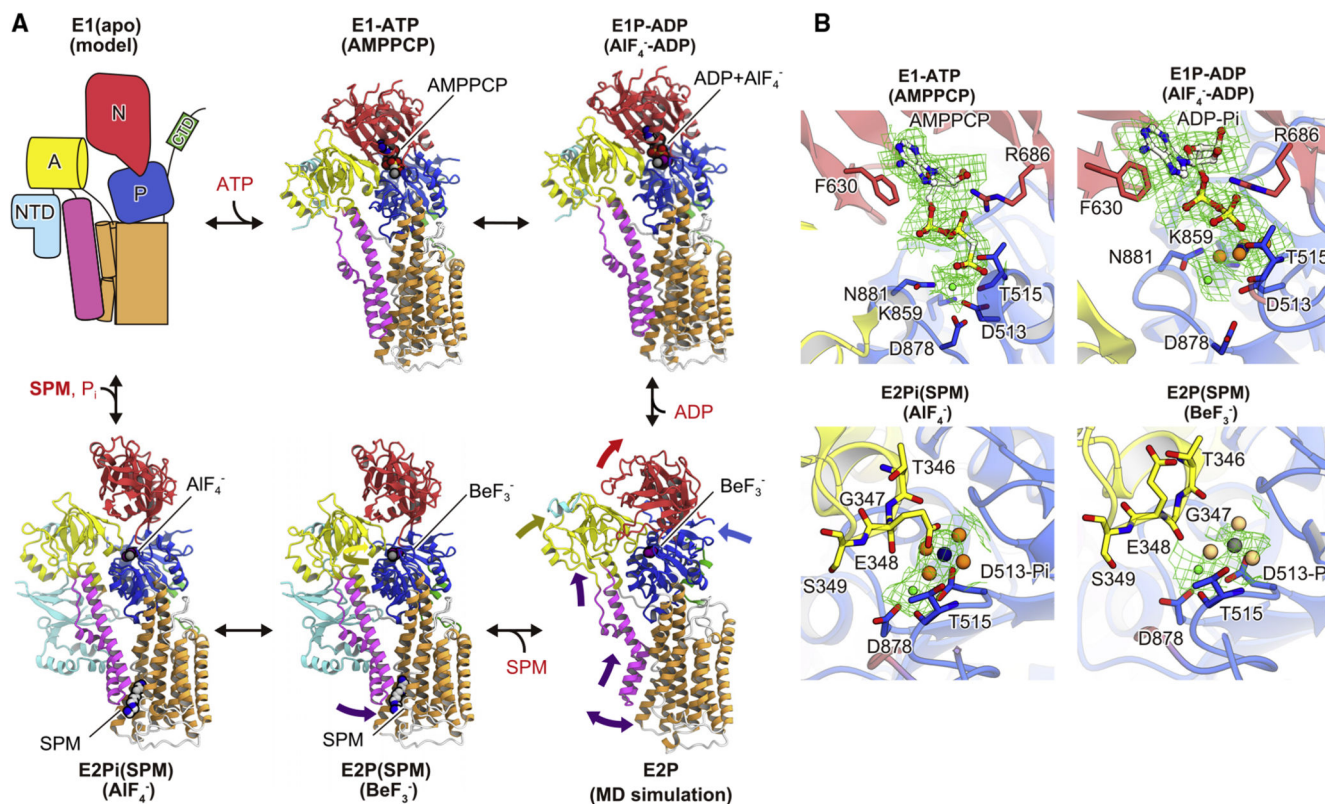
Figure 2. Conformational changes of ATP13A2 during the transport cycle

(A) Transport cycle of ATP13A2. Respective conformations are captured by AMPPCP (E1-ATP state), AlF_4^--ADP (E1P-ADP state), BeF_3^- (E2P(SPM) state), and AlF_4^- (E2Pi(SPM) state). The snapshot at 200 ns of the molecular dynamics (MD) simulation of the E2P state in the absence of SPM is indicated for the E2P state.

(B) Cryo-EM densities of the inhibitors are shown. AMPPCP and ADP are shown as sticks, and AlF_4^- and BeF_3^- are shown as spheres. Magnesium ion is shown as a small green ball. Densities are shown as green meshes, contoured at 3.5 σ. Residues involved in the inhibitor binding are shown in sticks.
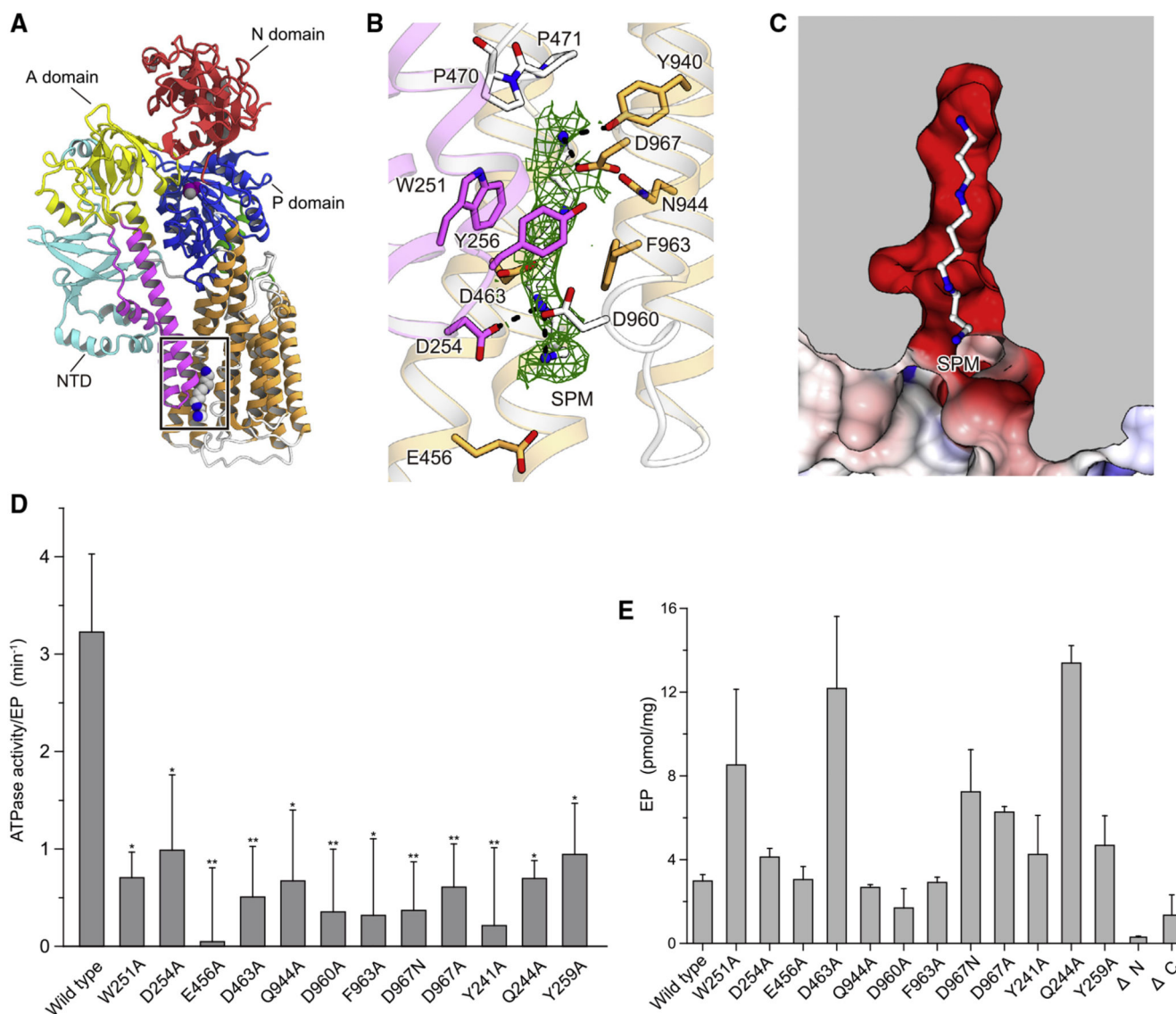
See also Figures S1-S5 and Data S1.

Figure 3. SPM recognition by ATP13A2

(A) Overall structure of ATP13A2 in the BeF$_3$ $^-$-stabilized SPM-bound state. The ribbon representation of the BeF$_3$ $^-$-bound state is viewed parallel to the membrane. The SPM-binding site is highlighted by a black rectangle.

(B) Close-up view of the SPM-binding site in the BeF$_3$ $^-$-bound ATP13A2 cryo-EM map. Amino acid residues involved in SPM recognition and two proline residues (Pro470 and Pro471) in the PPAL motif are shown as stick models. Dashed black lines indicate the hydrogen bonds between ATP13A2 and SPM.

(C) Cut-away molecular surface representation of the SPM-binding site. The molecular surface is colored according to the electrostatic potential, ranging from blue (+20 kT/e) to red (−20 kT/e), where kT is the thermal energy and e is the elementary charge.

(D) ATPase activities of ATP13A2 for the wild type and mutants. The SPM-dependent ATPase activities of each mutant are normalized by the amount of the phosphoenzyme (EP)

formation. These values show the turnover rates of the accumulated E2P in the wild type and mutants. The amount of EP formation for each mutant is shown in Figure 3E. Data represent the mean ± SEM of three to six measurements. Statistical significance compared with the wild type is shown: *$p < 0.05$; **$p < 0.005$.

(E) The amount of EP formation was measured using microsomes expressing wild type or mutant ATP13A2. Microsomes were incubated with [γ-^{32}P]ATP at 37°C for 1 min without substrate polyamines, but in the presence of 0.125 mM PIP$_2$ and 0.125 mM PA. Under these conditions, all of the mutants, as well as the wild type, accumulate the PE at the steady state. The steady level of EP reflects that of the active, expressed ATP13A2. The reaction was quenched with ice-cold trichloroacetic acid containing P$_i$. The amount of EP formation was determined as described in the STAR Methods. Data represent the mean ± SEM of three to five measurements.
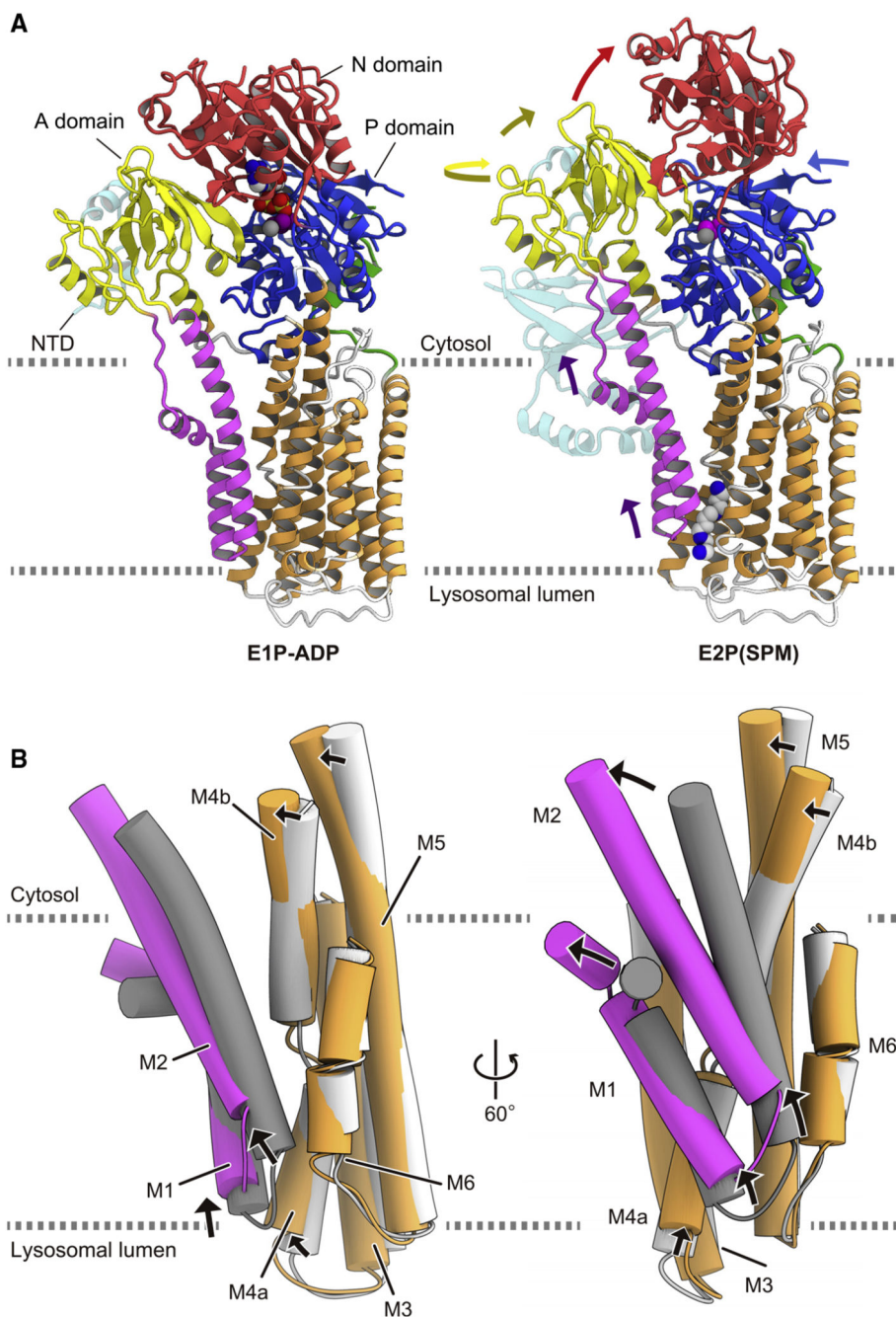
See also Figure S6 and Data S1.

Figure 4. Structural dynamics of E1P-ADP state to E2P(SPM) state transition in ATP13A2

(A) Ribbon model representation of the E1P-ADP state and the BeF_3^--bound E2P(SPM) state are shown. Structural changes of the A, N, and P domains and the M1−M2 helices are indicated by arrows with the same colors as the model.

(B) Close-up view of the TM segments. Conformational changes of M1−M6 from the E1P-ADP state (gray) to the E2P(SPM) state (colored). Structures are aligned on the M5−M10 helices. The rearrangements of the TM helices are indicated by black arrows.
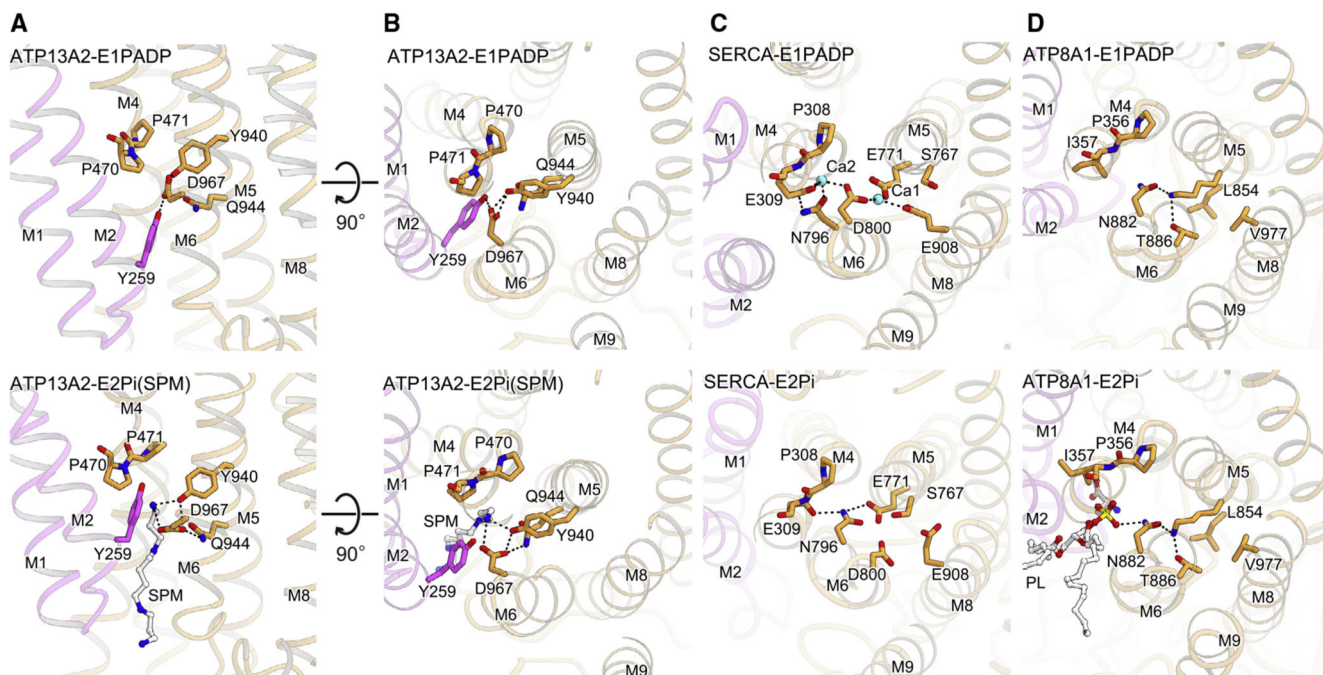
See also Figure S5.

Figure 5. Comparison of the substrate-binding sites

(A and B) Polyamine-binding site of ATP13A2 in the SPM-unbound state (top: E1P-ADP) and the SPM-bound state (bottom: E2Pi(SPM)), viewed from within lipid membrane (A) and from the cytoplasmic side (B). Residues involved in SPM transport are shown as ball-and-stick representations. Hydrogen bonds are shown as black dashed lines.

(C) Ca^{2+}/H^+-binding site of SERCA in the Ca^{2+}-bound state (top: PDB: 1T5T) and the counter-transporting H^+-bound state (bottom: PDB: 3B9R), viewed from the same viewpoints as in (B). Residues involved in the substrate binding are shown as ball-and-stick representations. Hydrogen bonds are shown as black dotted lines, and the bound Ca^{2+} ions are cyan spheres.

(D) Phospholipid-binding site of ATP8A1 in the E1P-ADP phospholipid-unbound state (top: PDB: 6K7K) and the E2Pi phospholipid-bound state (bottom: PDB: 6K7M), from the same viewpoints as in (B). Residues involved in phospholipid translocation are shown as ball-and-stick representations. Hydrogen bonds are shown as black dotted lines.

See also Figures S8 and S9 and Data S1.
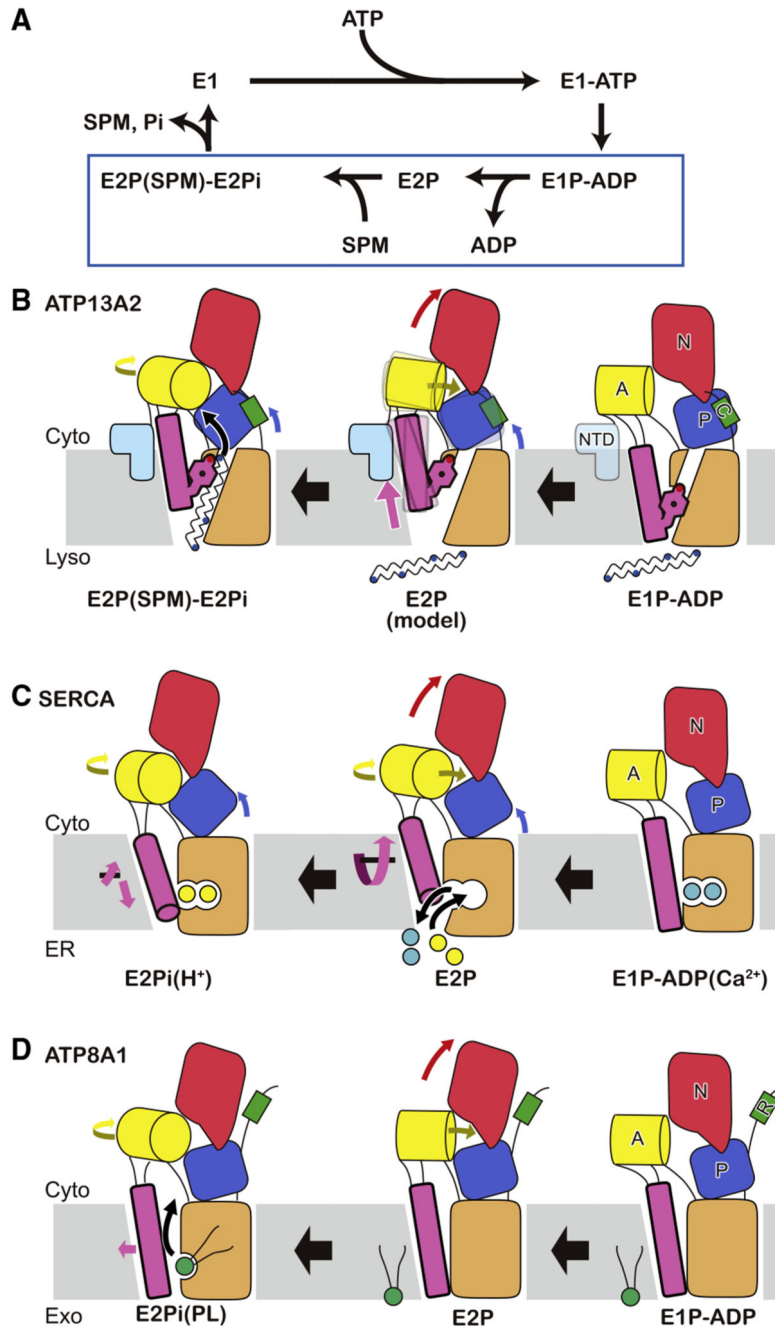
Figure 6. Proposed mechanism of SPM transport by ATP13A2

(A) Transport cycle of ATP13A2. The P-type ATPases generally follow the Post-Albers scheme. Phosphorylation induces the transition of the two states, E1 and E2, which are defined as high-affinity states for cytoplasmic and luminal/ extracellular substrates, respectively. Binding of the luminal/extracellular substrate (SPM in ATP13A2) requires sequential steps in most P-type ATPases, through E1P, E2P, and E2Pi intermediates, as indicated in the blue rectangle.

(B–D) Schematic models of luminal/extracellular substrate binding during the transport cycles in ATP13A2 (B), SERCA (C), and ATP8A1 (D). Rearrangements of the cytoplasmic domains are indicated by arrows. Domain movement is coupled to the phosphorylation and dephosphorylation of the P domain, which alternately changes the substrate affinity of the enzyme. Despite the overall similarity in the reaction scheme, there are variations in the conformational changes among the members.

See also Figures S7-S9.
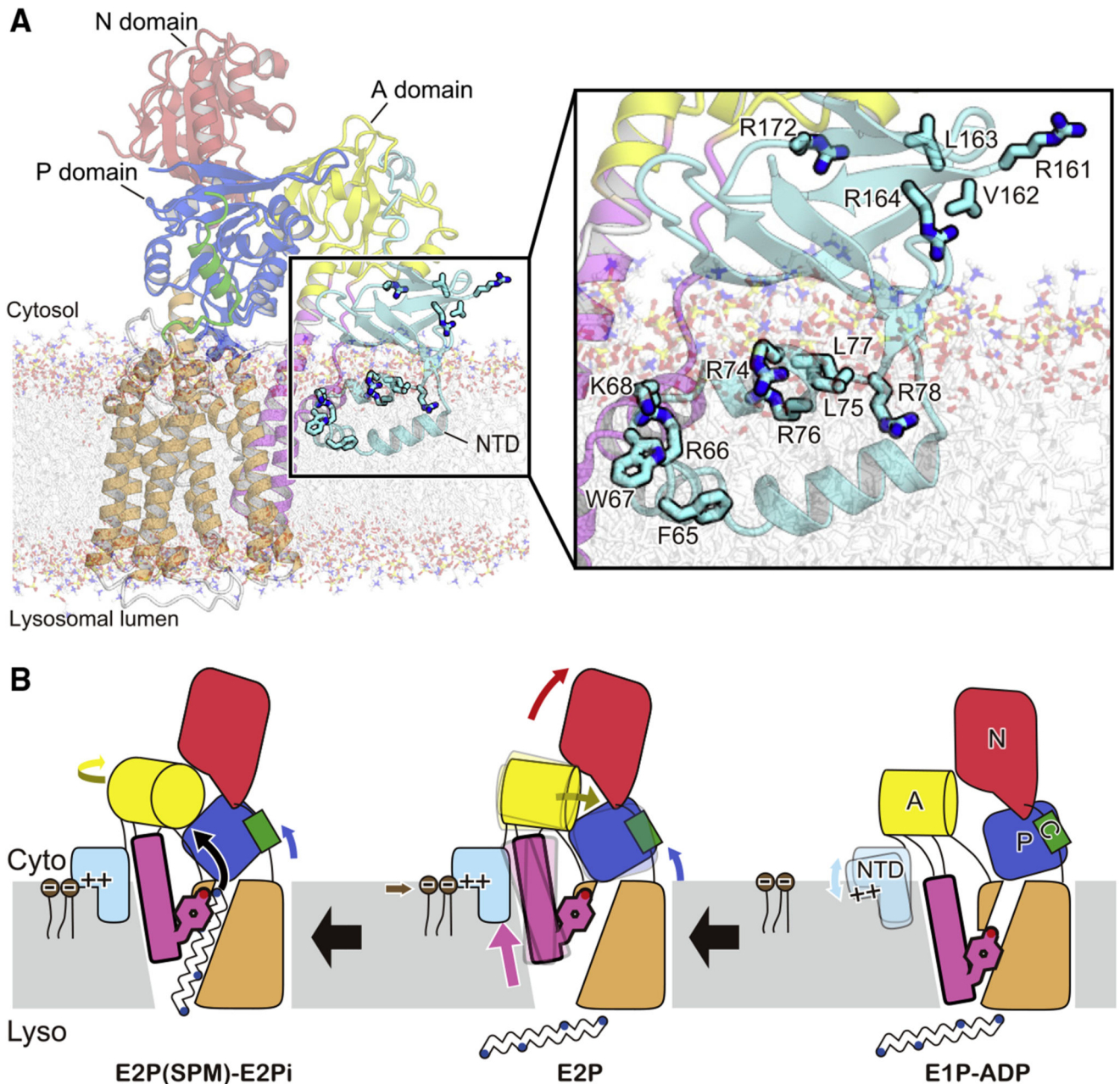
Figure 7. Proposed model for lipid-facilitated transport of ATP13A2 mediated by NTD

(A) ATP13A2 embedded in a lipid bilayer, using coarse-grained simulation, is shown. Lipids are shown in ball-and-stick representations. Amino acid residues in the predicted lipid-binding sites are shown in thick stick representations.

(B) Proposed model for the lipid-facilitated E1P-to-E2P transition during the transport cycles in ATP13A2. Binding of negatively charged lipids, such as PA and PIP_2, stabilize NTD to facilitate the E1P-to-E2P transition upon phosphorylation. Schematic model of ATP13A2 is illustrated as in Figure 6B, and PA and PIP_2 are shown in brown.

Key Resources Table

REAGENT or RESOURCE	SOURCE	IDENTIFIER
Antibodies		
GFP enhancer nanobody	Kirchhofer et al., 2010	PDB: 3K1K
Bacterial and virus strains		
Baculovirus	Thermo Fisher Scientific	10359016
Chemicals, peptides, and recombinant proteins		
Freestyle 293 medium	GIBCO	12338-018
Sf9-900 II SFM	GIBCO	10902-088
Spermine	Sigma-Aldrich	85590
N-dodecyl β-D-maltoside	Calbiochem	69227-93-6
Cholesteryl hemisuccinate	Anatrace	CH210
glyco-diogenin	Anatrace	GDN101
Ni-NTA Superflow resin	QIAGEN	30410
CNBr-activated Sepharose 4 Fast Flow Lab Packs	GE Healthcare Life Science	17098101
Superose 6 Increase 10/300 GL column	GE Healthcare	29091596
300 mesh R 1.2/1.3 holey carbon Cu/Rh	Quantifoil	https://www.quantifoil.com/products/quantifoil/quantifoil-circular-holes/
Critical commercial assays		
Bac-to-Bac Baculovirus Expression System	Invitrogen	A11098
Deposited data		
ATP13A2 coordinate (E1-ATP state)	This paper	PDB: 7VPI
ATP13A2 coordinate (E1P-ADP state)	This paper	PDB: 7VPJ
ATP13A2 coordinate (E2P(SPM) state)	This paper	PDB: 7VPK
ATP13A2 coordinate (E2Pi(SPM) state)	This paper	PDB: 7VPL
ATP13A2 map (E1-ATP state)	This paper	EMDB: EMD-32066
ATP13A2 map (E1P-ADP state)	This paper	EMDB: EMD-32067
ATP13A2 map (E2P(SPM) state)	This paper	EMDB: EMD-32068
ATP13A2 map (E2Pi(SPM) state)	This paper	EMDB: EMD-32069
Structure of the (SR) Ca^{2+}-ATPase $Ca2$-$E1$-ADP:AlF_4^- form	Sørensen et al., 2004	PDB: 1T5T
SERCA Ca^{2+}-ATPase E2 aluminum fluoride complex without thapsigargin	Olesen et al., 2007	PDB: 3B9R

REAGENT or RESOURCE	SOURCE	IDENTIFIER
Cryo-EM structure of the human P4-type flippase ATP8A1-CDC50 (E1-ADP-Pi state)	Hiraizumi et al., 2019	PDB: 6K7K
Cryo-EM structure of the human P4-type flippase ATP8A1-CDC50 (E2Pi-PL state)	Hiraizumi et al., 2019	PDB: 6K7M
Structure of P5A-ATPase Spf1, endogenous substrate-bound	McKenna et al., 2020	PDB: 6XMU
Cryo-EM structure of the human P4-type flippase ATP8A1-CDC50 (E1-ATP state class1)	Hiraizumi et al., 2019	PDB: 6K7J
Structure of the (SR) Ca^{2+}-ATPase Ca2-E1-AMPPCP form	Sørensen et al., 2004	PDB: 1T5S
Structure of P5A-ATPase Spf1, AMP-PCP-bound form	McKenna et al., 2020	PDB: 6XMQ
Structure of P5A-ATPase Spf1, BeF3-bound form	McKenna et al., 2020	PDB: 6XMT
Structure of the E2 beryllium fluoride complex of the SERCA Ca^{2+}-ATPase	Olesen et al., 2007	PDB: 3B9B
Experimental models: Cell lines		
HEK293S GnTI⁻		N/A
Oligonucleotides		
Primers for ATP13A2 mutants, see Table S1	This paper	N/A
Recombinant DNA		
pEGNGFP-HumanATP13A2	This paper	N/A
pET22b-GFP binding nanobody	This paper	N/A
Software and algorithms		
Refmac5	Nicholls et al., 2018	https://www.mrc-lmb.cam.ac.uk/groups/murshudov/content/refmac/refmac.html
ProSMART	Nicholls et al., 2012	https://www.mrc-lmb.cam.ac.uk/groups/murshudov/content/prosmart/prosmart.html
Servalcat	Yamashita et al., 2021	https://github.com/keitaroyam/servalcat
COOT	Emsley et al., 2010; Nicholls et al., 2018	https://www.mrc-lmb.cam.ac.uk/personal/pemsley/coot/
PHENIX	Afonine et al., 2018	https://phenix-online.org/
MolProbity	Chen et al., 2010	https://phenix-online.org/documentation/reference/molprobity_tool.html
UCSF-ChimeraX	Goddard et al., 2018	https://www.cgl.ucsf.edu/chimerax/
CueMol	N/A	http://www.cuemol.org
VMD	Humphrey et al., 1996	http://www.ks.uiuc.edu/Research/vmd/
MemProtMD	Stansfeld et al., 2015	http://memprotmd.bioch.ox.ac.uk/
CHARMM-GUI	Jo et al., 2008; Kim et al., 2017	https://www.charmm-gui.org/
NAMD2.13	Phillips et al., 2005	http://www.ks.uiuc.edu/Research/namd/

Table 1

Cryo-EM data collection and refinement statistics

	E1ATP		E1P-ADP	E2P(SPM)	E2Pi(SPM)
Data collection and processing					
EMDB-ID	EMD-32066		EMD-32067	EMD-32068	EMD-32069
PDB	7VPI		7VPJ	7VPK	7VPL
Inhibitor	AMPPCP		AlF_4^--ADP	$BeF3^-$	AlF_4^-
Microscope	Titan Krios G3i				
Detector	Gatan K3 camera with quantum LS energy filter				
Data acquisition mode	Counting mode			CDS counting mode	
Magnification	105,000				
Voltage (kV)	300				
Electron exposure ($e^-/Å^2$)	50		50	60	60
Defocus range (mm)	−0.8 to -1.6				
Pixel size (Å)	0.83				
Symmetry imposed	C1				
Number of movies	3,114		3,303	3,289	3,834
Initial particle images	1,989,286		1,950,094	1,762,758	1,958,257
Final particle images	59,432		121,731	15,602	18,347
Map resolution (Å)	3.60		3.54	3.92	3.78
FSC threshold	0.143				
Map sharpening B factor ($Å^2$)	−128.0		−148.0	−90.6	−93.2
Model building and refinement					
Model composition					
Protein atoms	7,343		7,343	8,150	8,150
Metals	1		2	2	2
Other atoms	31		44	45	46
RMSD					
Bond lengths (Å)	0.0172		0.0174	0.0175	0.0173
Bond angles (°)	2.37		2.38	2.29	2.29
Validation					
Clashscore	3.60		3.59	2.58	2.40
Rotamer outliers (%)	29.79		28.69	19.91	14.93
Ramachandran plot					
Favored (%)	95.58		95.48	95.98	96.94
Allowed (%)	4.00		4.10	3.92	2.97
Outliers (%)	0.42		0.42	0.10	0.10